VTT Technical Research Centre of Finland

Effect of hydrogen on electrochemical behavior of additively manufactured 316L in pressurized water reactor primary water

Bojinov, Martin; Saario, Timo; Ge, Yanling; Chang, Litao; Que, Zaiqing

Link to publication

Effect of hydrogen on electrochemical behavior of additively manufactured 316L in pressurized water reactor primary water

Martin Bojinov [a], Timo Saario [b], Yanling Ge [b], Litao Chang [c], Zaiqing Que [b,*]

[a] *Department of Physical Chemistry, University of Chemical Technology and Metallurgy, Kl. Ohridski Boulevard 8, 1756 Sofia, Bulgaria*
[b] *Advanced Materials for Nuclear Energy, VTT Technical Research Centre of Finland, Kivimiehentie 3, 02150 Espoo, Finland*
[c] *Shanghai Institute of Applied Physics, Chinese Academy of Sciences, 2019 Jialuo Road, 201800 Shanghai, China*

ARTICLE INFO

ABSTRACT

The electrochemical behavior of laser powder bed fusion (LPBF) 316 L stainless steel subject to different heat-treatments (solution annealing and hot isostatic pressing) is compared to nuclear-grade wrought 316 L in pressurized water reactor primary water at 288 °C (with and without dissolved hydrogen) using current-time transients, cyclic voltammetry and electrochemical impedance spectroscopy (EIS). Analysis of spectra by the Mixed-Conduction Model revealed slower corrosion rates of LPBF 316 L than wrought 316 L, the effect being more pronounced in the presence of dissolved hydrogen. The characteristics of the barrier layer and the oxide film/coolant interface were irreversibly altered upon removal of dissolved hydrogen.

1. Introduction

Additive manufacturing (AM) is an innovative technology used to fabricate complex-geometry and near-net-shape components with potentially minimal lead-time, final finishing and material waste [1,2]. Laser-based powder bed fusion (LPBF or PBF-LB) is currently one of the most widely employed AM techniques, the majority of trial AM materials for nuclear industry applications being based on that process [3–8]. With significant efforts being invested on processing, microstructural homogeneity and mechanical integrity of LPBF materials, components manufactured by LPBF have been deployed in commercial reactors since 2017. In 2022, the first additive manufactured stainless steel fuel debris filters were installed in nuclear power plants in Finland and Sweden [9, 9]. In light water reactors, components are subject to corrosion during their service in high-temperature water, which affects significantly the safe operation of nuclear power plants. Therefore, it is critical to understand the corrosion behavior of LPBF materials in reactor coolant environments and the underlying mechanisms.

Though a significant number of studies on the corrosion behavior of LPBF materials have been performed in the ambient temperature range, conclusions remain contradictory [10–12]. LPBF 316 L was reported to exhibit a wider passive potential range compared to wrought 316 L [13]. Passive layers formed on LPBF 316 L have been shown to have higher pitting resistance and higher stability than those on the wrought

material [14–16]. Conflicting results were reported by Nie [17] and Trelewicz [18], who observed a worse pitting resistance of AM 316 L compared to the wrought 316 L, resulting from either low OH⁻ concentration at boundaries or segregation of Mo and Cr.

Heat treatments are widely used to relieve residual stresses and eliminate microstructural and mechanical anisotropy in LPBF materials [19,20], which also influences the corrosion behavior [21]. Zhou [22], Shimada [23] and Laleh [24] reported that due to heat treatment, local elemental depletion resulting from coarsening/re-precipitation of inclusions can increase corrosion susceptibility. A contradictory role of heat treatment on electrochemical behavior was reported by Ettefagh [25] and Kong [26], claiming that post-AM heat treatments reduced corrosion rate of the AM stainless steel specimens. For application in nuclear sector, LPBF materials are required to be heat treated [8] and thus the impact of such treatment on electrochemical behavior in high-temperature water (270–325 °C) of LPBF stainless steel needs to be elucidated.

In the last few years, a couple of studies on corrosion resistance of AM stainless steels in high-temperature water were reported [7,8,21,27, 28]. However, with the notable exception of a pre-study conducted by some of the authors [29], there is no information to date on the high-temperature electrochemical behavior (> 280 °C) of post heat treated LPBF 316 L. No work has yet been reported to address the role of dissolved hydrogen on the high-temperature electrochemical response

of LPBF stainless steels. Several studies of the effect of dissolved hydrogen on oxide film growth and corrosion behavior of conventional 316 L stainless steel in pressurized water reactor (PWR) coolants have been reported [30–35]. It was concluded that oxide layers formed in de-aerated and hydrogenated water are rather similar in terms of chemical composition but quite different in morphology. The outer oxide particles formed on 316 L stainless steel in hydrogenated water were smaller and less sparse compared to those in de-aerated water. The apparent thickness of the whole oxide layer is somewhat larger in the presence of hydrogen. A thorough understanding of the electrochemical behavior of LPBF stainless steels in high-temperature water is crucial in assessing their performance and reliability in nuclear environments, particularly in PWR primary coolant containing hydrogen. From a methodological point of view, if water reduction / hydrogen oxidation reactions predominate over corrosion reactions, the extraction of parameters related to the latter becomes more difficult under hydrogenated conditions. Therefore, measurements in de-aerated solutions would be needed to estimate kinetic and transport properties more accurately. From a practical application point of view, since hydrogen feed in PWRs can be discontinuous, the effect of removing hydrogen from the coolant on electrochemical properties of materials should also be investigated.

In the present paper, the electrochemical behavior of two post-LPBF heat-treated 316 L materials and a reference nuclear-grade 316 L in a simulated PWR primary coolant with varying dissolved hydrogen amounts has been thoroughly investigated. In-situ measurements including re-passivation transients, electrochemical impedance spectroscopy (EIS) and current-potential curves were performed. EIS data were interpreted by the Mixed-Conduction Model (MCM) allowing for an estimation of kinetic and transport parameters of oxide film growth and restructuring. The impacts of heat treatment and dissolved hydrogen on composition, structure, and morphology of oxides on LPBF 316 L were also thoroughly studied.

2. Experimental

2.1. Materials

The LPBF specimens were printed by EOS M290 with nitrogen gas atomized 316 L powders (average diameter of 36 μm) in argon atmosphere with a ceramic re-coater blade and a building platform temperature of 80 °C. The printing parameters were taken from 316L_SurfaceM291 1.10 [36] with a printing layer thickness of 20 μm. The printed specimens were solution annealed (SA) or hot isostatic pressed (HIP) with the details shown in Table 1. The reference wrought 316 L material was fabricated by Creusot-Loire Industrie based on the RCC-M M3307 level 3 specifications. The chemical composition of LPBF 316 L powder and reference 316 L is shown in Table 2. The mechanical properties of the studied materials were thoroughly discussed in ref. [29] and found to fulfil the requirements specified by the procurement guideline on nuclear-grade 316 L stainless steel [37] [37].

2.2. Electrochemical measurements

Plate specimens with dimensions of $1 \times 1 \times 0.3$ cm were extracted by electrical discharge machining from the heat treated blocks in the build direction. Specimens for electrochemical measurements in simulated

Table 1
Parameters of the heat treatments utilized.

Designation	Detailed conditions
SA	Solution annealing at 1066 °C for 1 h in argon and then air cooling (AMS 2759)
HIP	Hot isostatic pressing at 1150 °C for 4 h in argon of 100 MPa and then furnace cooling

PWR coolant received a final polishing with 0.25 μm paste and an ultrasonic cleaning in ethanol. The electrochemical experiments were carried out in a 316 L autoclave attached to a recirculating loop. A beginning-of-cycle PWR water chemistry was utilized, i.e., 2.2 ppm Li (added as LiOH), 1000 ppm B (added as H_3BO_3), pH 7.0 at 288 °C, with or without 35 cm^3 of dissolved H_2 / kg H_2O (1.57 mmol kg^{-1} H_2). The water chemistry was monitored and recorded continuously. A Pt plate served as a counter electrode, whereas a Ni/NiO couple pH-electrode was employed as a reference. Voltammetric scans were performed in the interval of potentials $-0.1/1.0/-0.095$ V vs. that reference at a scan rate of 1 mV s^{-1}. All the potentials were corrected for the IR-drop as a product of the measured current density and the high-frequency intercept of the real part of impedance spectra and re-calculated to the standard hydrogen electrode (SHE) scale. EIS measurements were conducted at the open-circuit potential (E_{oc}), using an Ivium CompactStat potentiostat. The EIS measurements were performed over a frequency range of 100 kHz to 0.1 mHz, with an alternating current (ac) amplitude of 50 mV (rms). Spectra measured at selected conditions with amplitudes ranging from 20 to 50 mV were identical within the measurement error (± 1 % by magnitude and $\pm 2°$ by phase shift), indicating that linearity condition was satisfied. Causality of the impedance was checked via a Kramers-Kronig compatibility test using the measurement model and associated software [38] [38]. To study the influence of dissolved hydrogen on corrosion and re-passivation kinetics, a sequence of electrochemical measurements was adopted as follows:

1 PWR water with H_2 was circulated through the autoclave. The measurements started after the formation of a stable oxide layer (at least 48 h, following the EIS of the specimens until stabilized). Afterwards, re-passivation transients (with a measurement interval of 1 ms) and EIS of all specimens were recorded:

    1.1 Current-time curves during potential steps from –0.815 (0.5 s) to −0.565 V (8 s).

    1.2 Current-time curves during potential steps from –0.815 (0.5 s) to −0.465 V (8 s) Re-passivation potentials were selected in order not to change surface film composition via transpassive dissolution of Cr based on E-pH diagrams calculated by HSC software [39].

    1.3 EIS measurement at E_{oc} (–0.705 V).

2 Removal of H_2 in the high-temperature water by N_2 bubbling through the feed water tank. Nitrogen was added until the stabilization of EIS of the specimens. Residual H_2 concentration was less than 0.03 cm^3 / kg H_2O.

3 Re-passivation transients and EIS of all specimens were measured in the following order.

    3.1 EIS measurement at E_{oc} (E_{oc} after H_2 removal was −0.64 V).

    3.2 Current-time curves during potential steps from –0.815 (0.5 s) to −0.565 V (8 s).

    3.3 Current-time curves during potential steps from –0.815 (0.5 s) to −0.465 V (8 s).

4 Restoring the dissolved hydrogen concentration by H_2 bubbling through the feed water tank. Stabilization of the EIS of at least one of the specimens was sought before further measurements were started.

    4.1 EIS measurement at E_{oc} (–0.705 V).

    4.2 Current-time curves during potential steps from –0.815 (0.5 s) to −0.3 V (8 s).

    4.3 Polarization at −0.815 V for 600 s, then cyclic voltammetry (CV) in the –0.815 / 0.30 / −0.815 V interval (sweep rate 1 mV s^{-1}).

The corrosion behavior of the studied materials is determined by the field strength and diffusion coefficients in the passive film, as well as by the charge transfer rate constants at the oxide film/ solution (F/S) and metal /oxide (M/F) interfaces. These parameters were estimated through the use of a complex non-linear least-squares method based on the Levenberg-Marquardt algorithm, via fitting the EIS data to the MCM [29,40,41]. To ensure parameter viability, statistical weighting was applied for all datasets, and the estimation errors were multiplied by the reduced values of χ^2 derived from the regression. For obtaining valid statistical values for all parameters, parameters with a mutual

Table 2

Chemical compositions (wt%) of the nuclear-grade wrought 316 L material and the LPBF 316 L powder utilized.

	Fe	Cr	Ni	Mo	Mn	Si	N	Cu	C	S	P
Wrought 316L	Bal.	17.3	11.5	2.6	1.8	0.37	0.05	0.024	0.027	0.004	0.03
LPBF 316L powder	Bal.	17.9	13.0	2.7	1.5	0.25	0.07	<0.01	0.005	0.005	<0.01

dependence greater than 0.67 were never simultaneously fitted.

2.3. Characterization of oxide microstructure

The cross-sectional samples were polished to a surface finish of 0.05 μm using oxide suspension. Baseline microstructural characterization was performed using a Zeiss Crossbeam 540 scanning electron microscope (SEM) with a four-quadrant backscatter detector and an EDAX HikariPlus electron backscatter diffraction (EBSD) detector. Secondary electron (SE) and backscattered electron (BSE) mode were used for SEM imaging. EBSD was performed with the samples tilted at 70°, a working distance of 12–14 mm and a step size of 100 nm. The resulting EBSD inversed pole figure (IPF) and kernel average misorientation (KAM) maps were analyzed. The in-depth elemental composition of the oxide layers was analyzed using Energy Dispersive X-Ray (EDX) spectroscopy.

To assess the detailed microstructures at the F/S and M/F interfaces formed in PWR water, lamellae were extracted using focused ion beam (FIB) nanofabrication by JEOL JIB 4700. The lamellae were analyzed using a Thermal Fisher Talos F200X analytical transmission electron microscope (TEM) with Super-X (4 SDDs) operated at 200 kV. The grains of interest were tilted to obtain selected area electron diffraction (SAED) along crystallographic zone-axes. Bright field (BF) and high-angle annular dark-field (HAADF) images were taken. Spectral images were collected to reveal chemical composition for all phase in scanning TEM (STEM) mode [42].

3. Results

3.1. Characterization of base materials

Fig. 1 shows the EBSD IPF, grain boundaries and pattern quality overlaid maps and KAM maps for the wrought 316 L, SA and HIP treated LPBF 316 L materials. The wrought material exhibits equiaxed grains with high-angle grain boundaries (HAGBs) and twin boundaries within
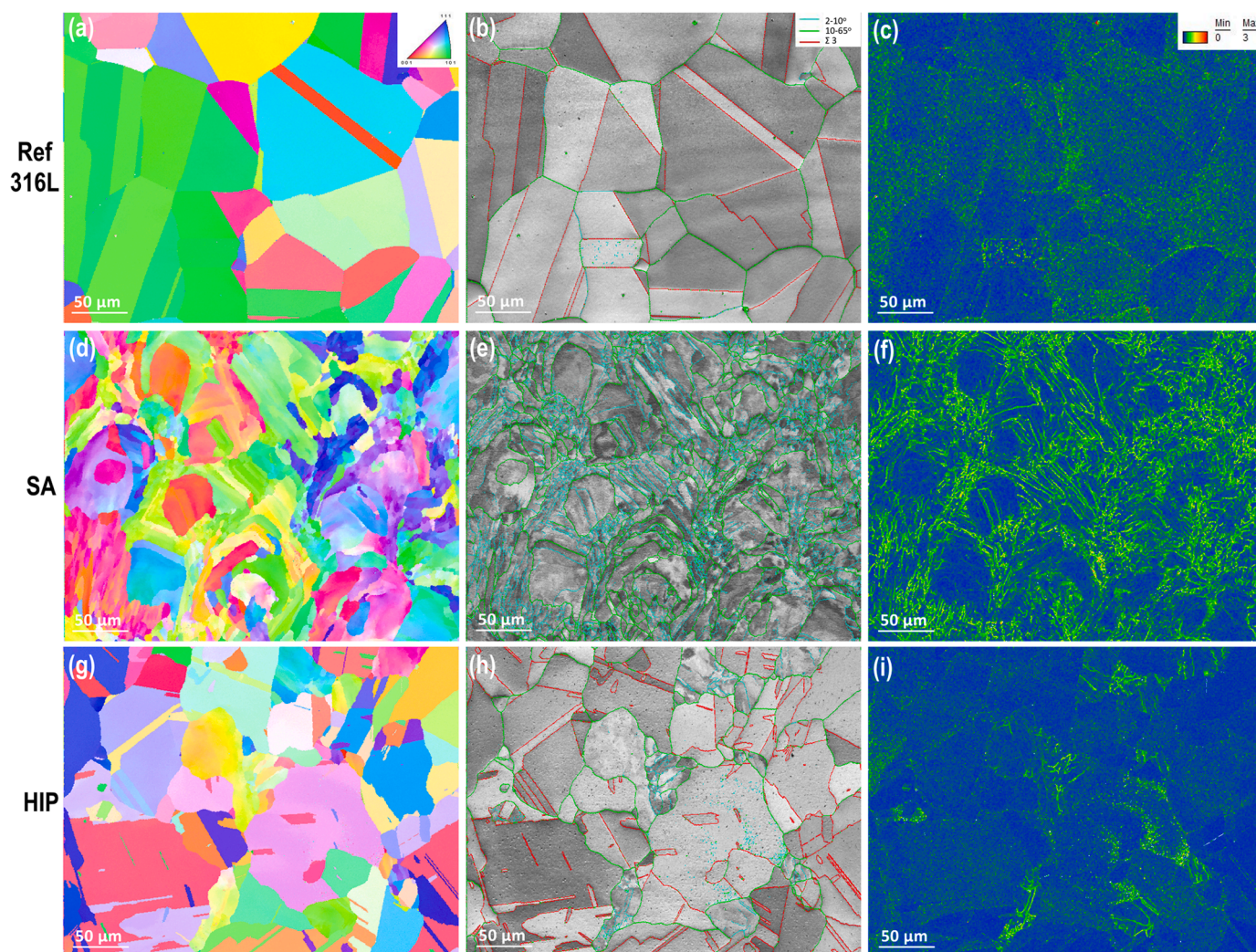

Fig. 1. (a, d, g, j) IPF maps, (b, e, h, k) image quality and grain boundaries overlaid maps and (c, f, i, l) KAM maps for (a-c) wrought 316 L, (d-f) SA and (g-i) HIP materials.

the grains (Fig. 1(b-c)). In the SA treated sample columnar-shaped fine grains were observed. The majority of its grain boundaries were low-angle grain boundaries (LAGBs) (Fig. 1(e)). A high geometrically necessary dislocation density was revealed within the grains by KAM map (Fig. 1(f)). In the HIP-treated sample, recrystallization occurred in most areas, resulting in a microstructure of equiaxed grains with HAGBs and the formation of twin boundaries within grains (Fig. 1(g-i)). However, local areas with grains that were not fully recrystallized still existed after the HIP process. The equiaxed grain size of the HIP treated sample was slightly smaller than that of the wrought 316 L (85 μm vs. 115 μm). The SA and HIP treated samples have a recovered and partial recrystallized microstructure, respectively. The fractions of LAGBs for the wrought 316 L, SA and HIP treated LPBF 316 L are 4.5 %, 72.4 % and 19.9 %, respectively. The fractions of HAGBs are 95.5 %, 27.6 % and 80.1 %, respectively. 61.6 %, 2.2 % and 79.6 % of the HAGBs are twin boundaries in these materials, respectively.

A complete recrystallization in LPBF 316 L was not achieved even with a HIP treatment. The higher resistance to recrystallization in LPBF 316 L compared to conventional 316 L material is attributed to dislocations cell structures without orientation change within the grains and the pinning by nano-precipitates to the movement of grain boundaries [43].

3.2. Re-passivation transients, CV, and EIS measurements

Re-passivation transients of the investigated materials are shown in Fig. 2 in log(current density) – reciprocal charge (q^{-1}) coordinates allowing estimation of a re-passivation parameter (*cBV*) according to the equation [44]:

$$\log i(t) = \log A + \frac{cBV}{q(t)} \tag{1}$$

where *V* is the step potential, *A* and *B* are parameters associated with the activation energy of mobile ion migration through the oxide film, *c* = $zF\rho/2.3 M$, *z* being the number of transferred electrons during oxidation, ρ the oxide density and *M* its molar mass.

The *cBV* values are collected in Table 3 depending on the type of material, step potential value and the presence/absence of hydrogen. They agree by order of magnitude with those measured recently for Alloy 690 in primary PWR coolant at 275 °C [45]. As indicated by *cBV* values, re-passivation rates of LPBF materials and wrought 316 L are roughly similar. The re-passivation parameter values are significantly higher only when a step towards a considerably more positive potential (−0.3 V) is performed, indicating a possible stress corrosion cracking (SCC) susceptibility in this region. This result is consistent with re-passivation rate measurements of Alloy 800 in primary PWR coolant containing different amounts of dissolved hydrogen and/or oxygen at 300 °C [46].

A comparison of cyclic voltammograms for wrought 316 L and LPBF 316 L, registered after a H_2 - no H_2 H_2 - H_2 sequence, is shown in Fig. 3. The current densities of wrought 316 L are comparable to those of the LPBF steels, with the notable exception of the HIP sample, for which current densities in both branches of the curve are considerably lower, and transpassive oxidation starts at a higher potential. In the negative-going sweep, also the current densities for SA material are somewhat lower than those of wrought 316 L.

Impedance spectra of the investigated materials in the presence and absence of H_2, as well as after a H_2 - no H_2 - H_2 sequence are shown in Figs. 4–6, respectively, in both complex plane and Bode coordinates. Nuclear-grade wrought 316 L material displays a higher corrosion rate than LPBF samples in the presence of dissolved H_2, as indicated by a lower impedance magnitude $|Z|_{f\to0}$ at the low-frequency end (i.e., lower polarization resistance). When dissolved hydrogen is purged from the system by N_2, $|Z|_{f\to0}$ of all materials increases by more than an order of magnitude, and differences between them tend to be less evident. The

impedance spectra in simulated PWR primary coolant without hydrogen are closely similar to earlier results for conventional 316 L at 280 °C [47]. It is also important to mention that the oxidized materials do not return to their original state after a further H_2 injection, even if the initial level of hydrogen is restored. Thus, the properties of both the barrier layer and the F/S interface are irreversibly altered when dissolved hydrogen is removed. It is important to mention that comparison between alloys based on $|Z|_{f\to0}$ is only tentative since the real polarization resistance can only be estimated via extrapolation based on model calculations.

A deconvolution of the spectra revealed the presence of four processes, characterized by their time constants. The time constant at the highest frequency typically corresponds to the barrier layer electronic properties. The two intermediate-frequency time constants are associated with charge transfer reactions at the F/S interface, whereas the low-frequency time constant is linked to transport of ionic defects through the barrier layer, which dominates the response. The estimation of kinetic parameters associated with interfacial reactions and ionic defect transport is discussed in Section 4.1.

3.3. Characterization of oxide films

3.3.1. Overall oxide film features

Fig. 7 displays SEM images of the oxidized surfaces on reference wrought and LPBF 316 L specimens after exposure to PWR coolant. The outer oxide layers on the SA and HIP treated LPBF specimens exhibited randomly distributed and dispersed oxide particles of similar size. A denser outer oxide layer is observed on the wrought 316 L sample (Fig. 7 (a, d, g)). As revealed in Fig. 7(b-c), partial dissolution was found on the wrought 316 L but not on heat-treated LPBF 316 L specimens.

Cross-sectional SEM-SE and BSE images of the outer and inner oxide layers of AM 316 L and NG wrought 316 L specimens after exposure to PWR environment are shown in Fig. 8. A bilayer structure composed of an inner and an outer layer was observed on all specimens. The wrought 316 L specimen exhibited a thicker and more uniform inner oxide layer, in contrast to the disperse and uneven inner oxide patches observed on SA and HIP treated LPBF specimens. At certain locations, a very thin inner oxide layer of ~70 nm was present for the AM specimens. The cross-sectional SEM-EDX maps of oxide layers on post heat-treated LPBF 316 L and nuclear-grade wrought material (Fig. 9) revealed a depletion of Fe and Ni and enrichment of Cr in the inner oxide layers.

3.3.2. Analytical electron microscopic studies of HIP sample

TEM analysis was conducted to examine in detail the M/F interface and the barrier layer between inner and outer oxides on the HIP treated LPBF sample. Fig. 10(a, b) illustrates that the outer oxide layer on the HIP specimen had sparsely distributed faceted crystallites. Most part of the inner layer was around 50–60 nm thick and only a single thicker inner oxide region (ca. 450 nm) was found in the lamella. Fig. 10(c, d) showed a segregation line, which was very close to the outer oxide interface, indicating a thin barrier layer on the HIP specimen. The SAED pattern of the outer oxide confirmed the FCC spinel structure along the zone axis (ZA) [114] with a lattice constant of ca. 8.57 Å. The ring pattern of the inner oxide was also FCC spinel with a lattice constant close to 8.52 Å. Fig. 10(e) shows the HRTEM image from the thicker inner oxide area, in which the yellow framed region was from the outer oxide, its fast Fourier transformation (FFT) being in line with the SAED pattern. The blue framed area was from the segregation line and showed a well crystallized structure in contrast to the surrounding amorphous phase. The FFT confirmed a spinel lattice along the ZA [112]. Fig. 10(f) was from a very thin inner oxide area including both the inner oxide/ outer oxide interface and the M/F interface. The blue framed area shows the M/F interface, in which FFT corresponded to a single orientation along the ZA [125] of spinel. The upper left FFT was from the whole imaged area and the indexation for the outer oxide was along the ZA [114] of spinel. The FFT of the yellow framed area at the inner oxide/
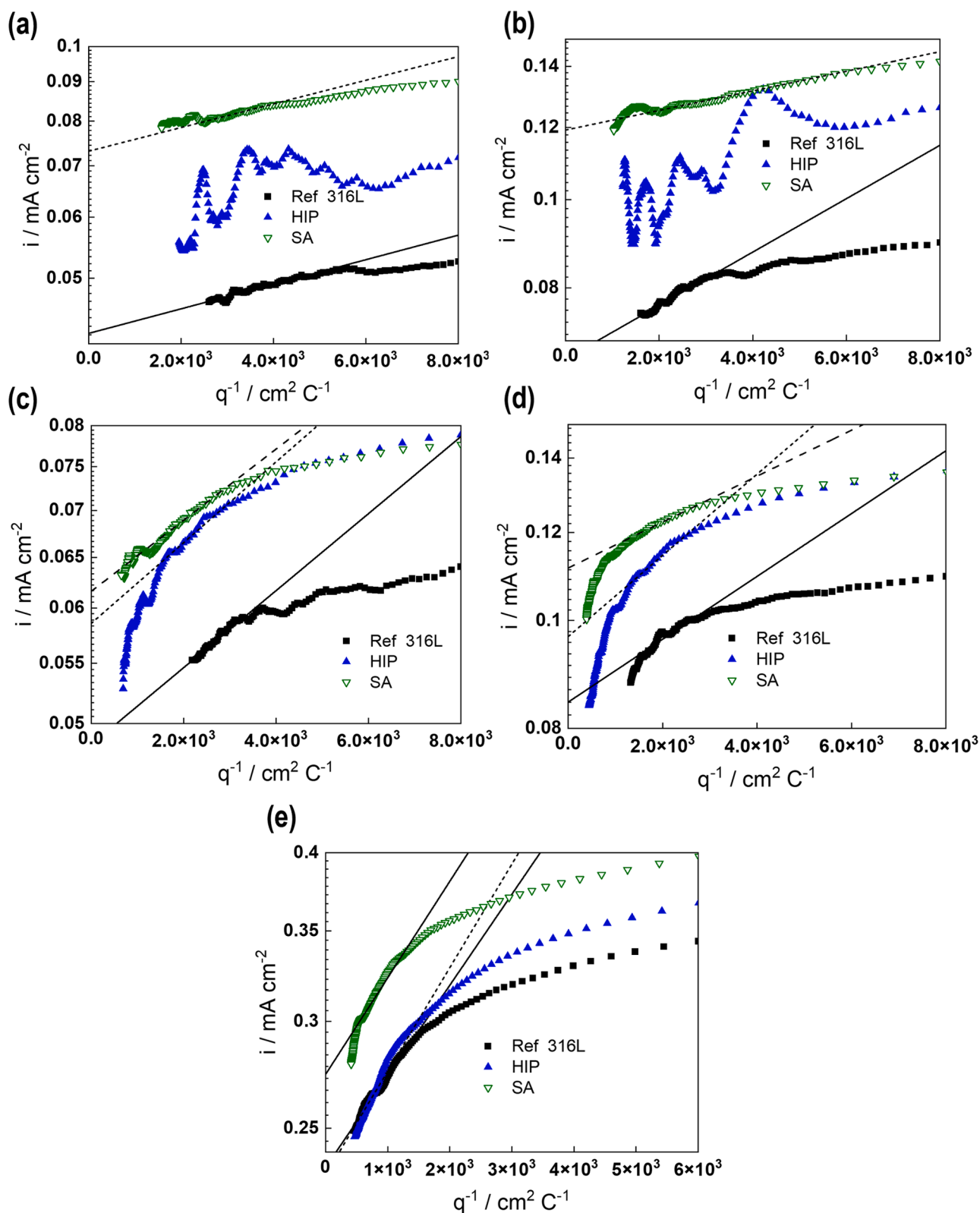
Fig. 2. Current-time transients during potential steps from –0.815 to –0.565 (a,c) and –0.465 V (b,d) in the presence (a,b) and absence (c,d) of dissolved H₂, (e) current-time transients during steps from –0.815 to –0.3 V after a sequence of H₂ - no H₂ - H₂. Semi-logarithmic current density(i) vs. reciprocal charge density (q⁻¹) coordinates used to estimate the cBV parameter (see text).

Table 3

Re-passivation parameter (cBV, cm2 mC-1) for the studied materials as depending on re-passivation potential in the presence and absence of dissolved H2.

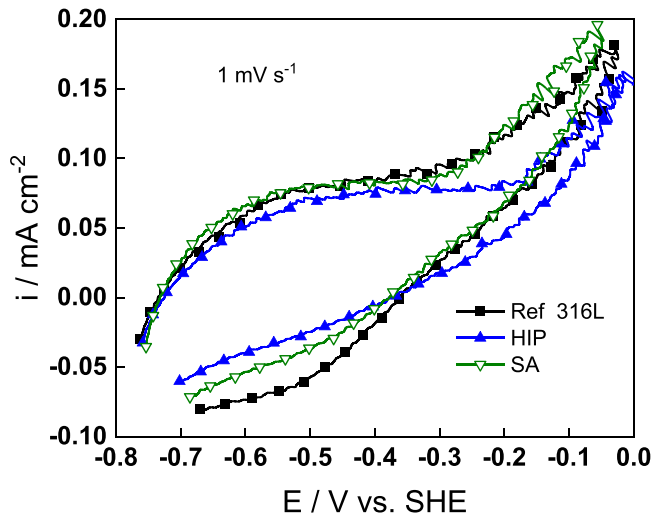| Material	With H_2		Without H_2		w.H_2 / without H_2 / w. H_2
E / V	−0.565	−0.465	−0.565	−0.465	−0.30
Wrought 316L	0.016	0.029	0.026	0.028	0.067
SA	0.015	0.011	0.024	0.020	0.071
HIP	0.017	0.020	0.027	0.036	0.072

Fig. 3. Cyclic voltammograms of the studied materials after a H_2 - no H_2 - H_2 sequence (sweep rate 1 mV s^{-1}). Potential values corrected with the IR drop estimated from EIS data.

outer oxide interface, was characteristic of a mixture of the outer and inner oxide, i.e. an overlap of ZA [125] and ZA [114]. This indicated that the inner layer had a large single grain mixed with amorphous phase. Based on the HRTEM studies for this material, it can be concluded that the barrier layer shows a well-defined crystal structure. The area with a thin inner oxide had larger nano-grains (> 10 nm) in comparison to those in the thicker inner layer region (< 10 nm).

Fig. 11 displays the morphology and composition of the outer and inner layers in the thick and thin inner oxide regions on the HIP material. The outer oxide layer was identified as a Fe-dominated spinel with local variations in Ni content, with a Fe to Ni ratio ranging from 3:1–9:1. The inner oxide layer was Cr-enriched spinel containing Fe and Ni, with a ratio of Cr/Fe/Ni approximately (4–5):2:1. At the segregation line, both Fe and Ni were enriched while Cr and Mn were depleted. The barrier layer was 15–40 nm thick over thin inner oxide area and 20–30 nm thick over thicker inner oxide regions. The dislocation arrays were clearly overlapping with the M/F interface, which suggested that the inner oxide formation process was directly related to dislocations and nano-precipitates in the matrix. In addition to the segregation line near the M/F interface, a few extra segregation lines were found in the thick inner oxide region, and their profiles were parallel to the side wall of the interface to matrix, as can be inferred from Fig. 11(a, b). This could be related to a sequential internal oxidation process which leads to a local step-by-step increase of inner oxide thickness. Mn-enriched particles are observed in the thin inner layer (Fig. 11(d)), at the same level as the segregation line. This suggests that nano-precipitates affect the oxide formation and segregation in the inner oxide layer.
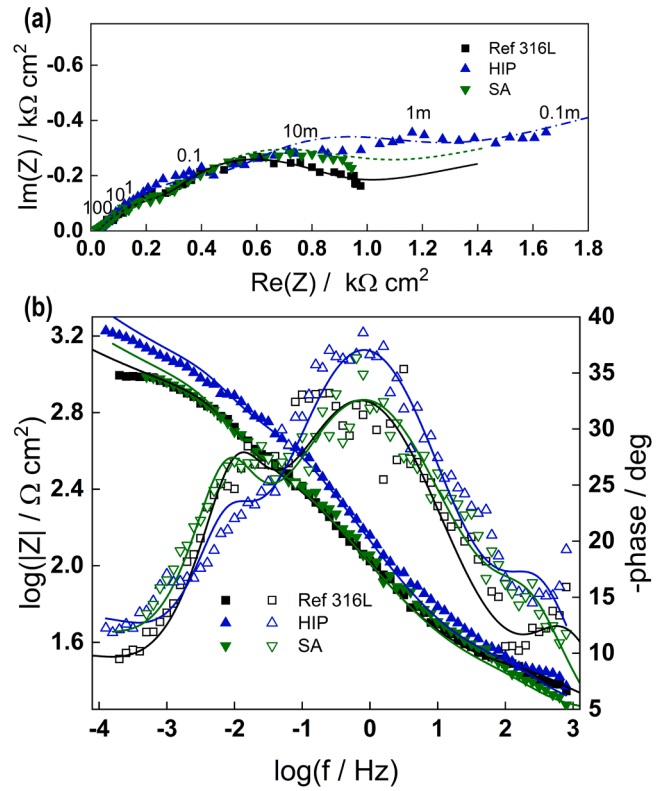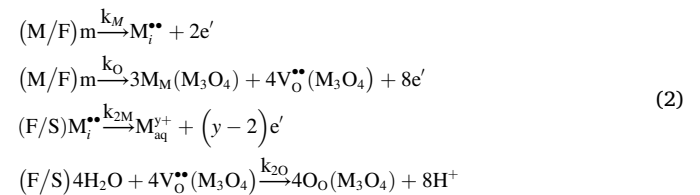

Fig. 4. Impedance spectra of the studied specimens in the presence of H_2, presented in (a) complex plane (parameter is frequency in Hz) and (b) Bode coordinates. Points – experimental data, lines - best-fit calculations based on the MCM.

4. Discussion

4.1. EIS data interpretation

As mentioned above, EIS data were quantitatively interpreted using the MCM. According to the model, the reactions occurring at the M/F interface and F/S interface are as follows:

$$(M/F)m \xrightarrow{k_M} M_i^{\bullet\bullet} + 2e'$$
$$(M/F)m \xrightarrow{k_O} 3M_M(M_3O_4) + 4V_O^{\bullet\bullet}(M_3O_4) + 8e'$$
$$(F/S)M_i^{\bullet\bullet} \xrightarrow{k_{2M}} M_{aq}^{y+} + (y-2)e'$$
$$(F/S)4H_2O + 4V_O^{\bullet\bullet}(M_3O_4) \xrightarrow{k_{2O}} 4O_O(M_3O_4) + 8H^+$$

$$(2)$$

in which *m* denotes an alloying atom (Fe, Cr or Ni) present in steel, while the remaining symbols follow the Kroger-Vink notation. The reactions at the interfaces are coupled via diffusion-migration of metal and oxygen through the barrier layer via interstitial cations and anion vacancies. Accordingly, the transfer function describing the impedance spectra can be written as:

$$Z = R_{el} + Z_{F/S} + Z_f \quad (3)$$

The water reduction/hydrogen oxidation reaction at the F/S interface is assumed to obey a Volmer-Heyrovsky mechanism:

$$H_2O + e^- \underset{k_{-1H}}{\overset{k_{1H}}{\rightleftharpoons}} H_{ad}(\theta) + OH^-$$
$$H_{ad}(\theta) + H_2O + e^- \underset{k_{-2H}}{\overset{k_{2H}}{\rightleftharpoons}} H_2 + OH^-$$

$$(4)$$

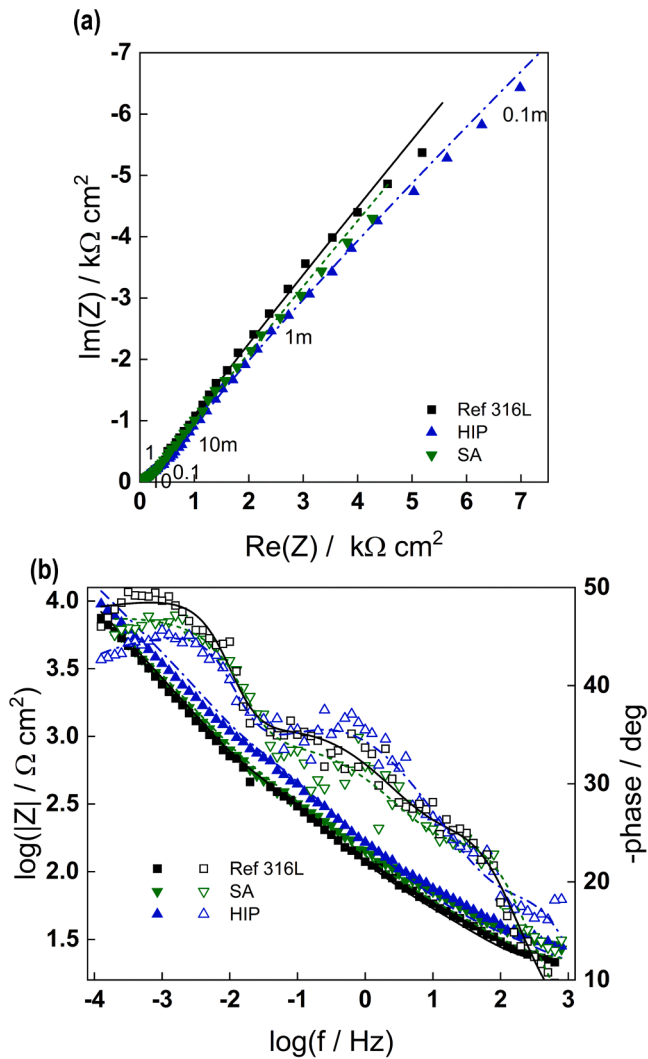with θ the surface coverage by atomic hydrogen (H_{ad}). Assuming

Fig. 5. Impedance spectra of the studied specimens in the absence of H_2, presented in (a) complex plane (parameter is frequency in Hz) and (b) Bode coordinates. Points – experimental data, lines - best-fit calculations based on the MCM.

exponential dependences of the rate constants on applied potential:

$$k_i = k_i^0 \exp\left(\pm \alpha \alpha_i \frac{F}{RT} E \right), i = 1H, -1H, 2H, -2H, 2M \tag{5}$$

with α representing the part of potential consumed at the F/S interface, and α_i - the respective transfer coefficients. Consequently, the F/S interface impedance can be expressed as:

$$Z_{F/S} = \frac{1}{Z_{f,\,F/S}^{-1} + j\omega C_{F/S}} \tag{6}$$

with:

$$Z_{f,F/S}^{-1} = R_{F/S}^{-1} + \frac{AX}{Z + j\omega\beta}$$

$$R_{F/S}^{-1} = F(k_{-1H}b_{-1H} + k_{2H}b_{2H})\overline{\theta} + F(k_{2H}b_{2H}c_{H_2} + k_{1H}b_{1H} + (y-2)k_{2M}b_{2M})(1-\overline{\theta})$$

$$A = F(k_{1H} + k_{-1H} - k_{-2H}c_{H_2} - k_{2M} - k_2)$$

$$X = k_{-2H}b_{-2H}c_{H_2} - (k_{-2H}b_{-2H}c_{H_2} - k_{1H}b_{1H} + k_{-1H}b_{-1H} - k_{2H}b_{2H})\overline{\theta} - k_{1H}b_{1H}$$

$$\overline{\theta} = \frac{k_{2H}c_{H_2} + k_{1H}}{Z}, Z = k_{-2H}c_{H_2} + k_{1H} + k_{-1H} + k_{2H}$$
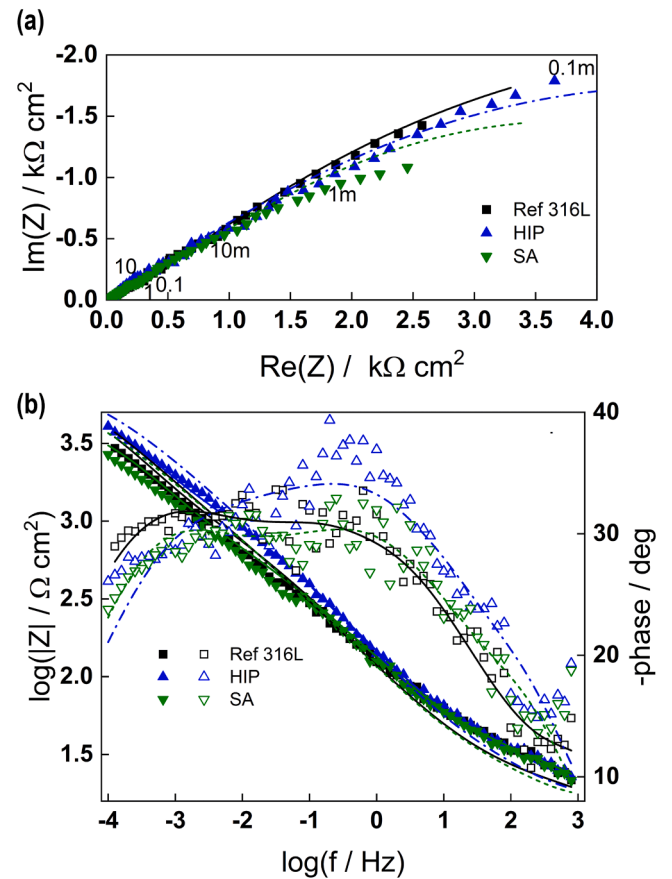
$$\tag{7}$$

Fig. 6. Impedance spectra of the studied specimens after a H_2 – no H_2 – H_2 sequenc, presented in (a) complex plane (parameter is frequency in Hz) and (b) Bode coordinates. Points – experimental data, lines - best-fit calculations based on the MCM.

The impedance of the oxide layer can be written as a linear combination of the impedance of its electronic properties (Z_e) and two ionic transport impedances related to interstitial cations ($Z_{ion,M}$) and oxygen vacancies ($Z_{ion,O}$):

$$Z_f = \left(Z_e^{-1} + Z_{ion,O}^{-1} + +Z_{ion,M}^{-1} \right)^{-1} \tag{8}$$

where:

$$Z_e \approx \frac{RT}{2j\omega F \overrightarrow{E} L C_{sc}} \ln \frac{[1 + j\omega \rho_d \varepsilon \varepsilon_0 \exp(2KL)]}{1 + j\omega \rho_d \varepsilon \varepsilon_0}, K = \frac{F}{RT}\overrightarrow{E}, \rho_d$$

$$= \frac{RT}{F^2 D_e} \frac{k_{2O} + k_{2M}}{k_O + k_M} \tag{9}$$

$$Z_{ion,O} \approx \frac{RT}{4F^2 k_O \left(1-\alpha\right)\left(1 + \sqrt{1 + \frac{4j\omega}{D_O K^2}}\right)}, Z_{ion,M}$$

$$\approx \frac{RT}{4F^2 k_M \left(1-\alpha\right)\left(1 + \sqrt{1 + \frac{4j\omega}{D_M K^2}}\right)} \tag{10}$$

in which D_O, D_M and D_e represent the diffusion coefficients for oxygen vacancies, interstitial cations and electronic carriers, respectively. The barrier layer thickness is denoted by L, while ε represents the dielectric constant and $\overrightarrow{E}$ - the field strength in the barrier layer. Therefore, the total impedance can be expressed as:

$$Z = R_{ohm} + \left(Z_e^{-1} + Z_{ion,O}^{-1} + Z_{ion,M}^{-1} \right)^{-1} + Z_{F/S} \tag{11}$$

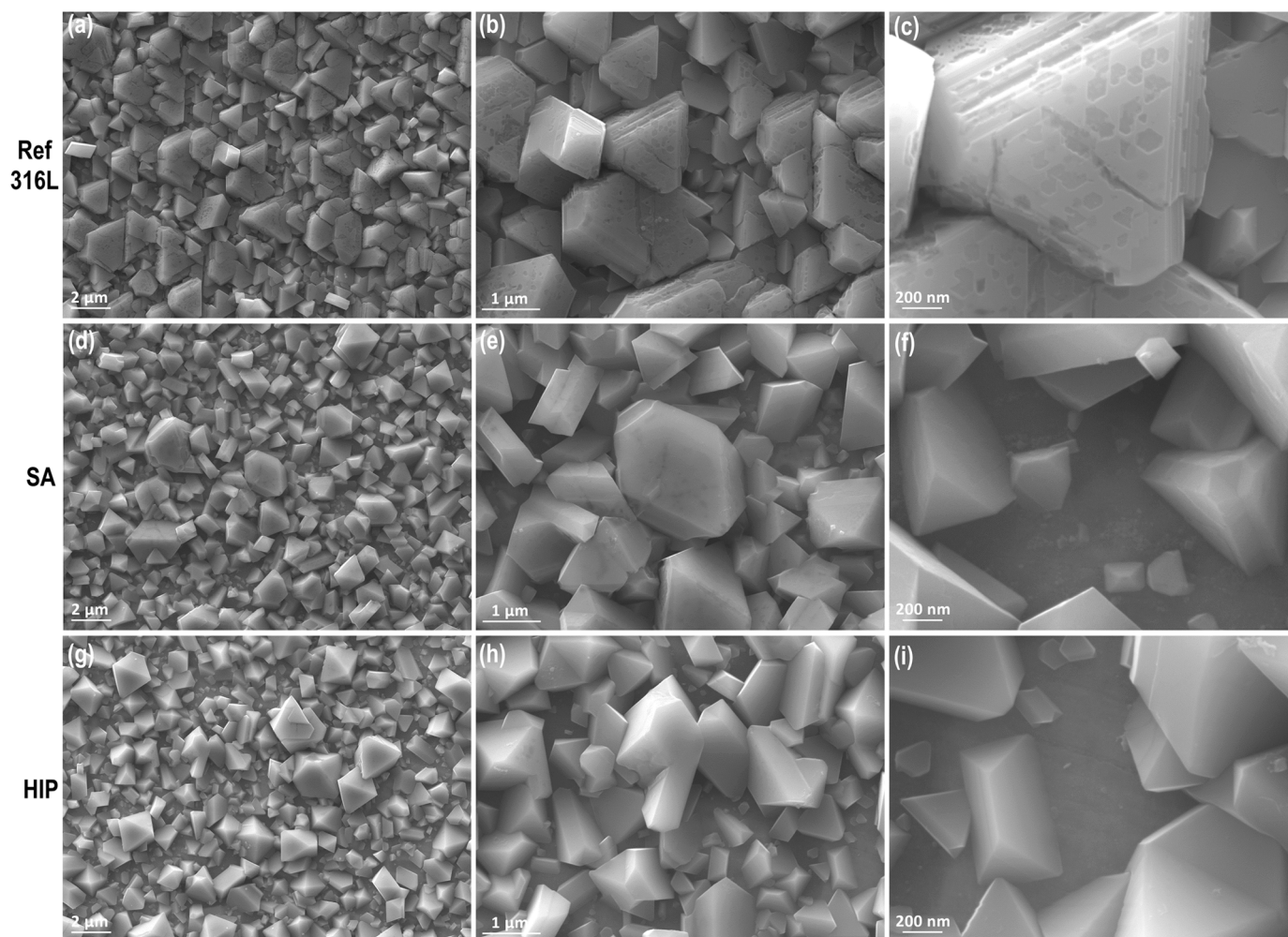The corresponding equivalent circuit that illustrates the connection

Fig. 7. The outer oxides on LPBF 316 L and wrought 316 L materials after electrochemical measurements in simulated PWR coolant. (a-c) Wrought 316 L; (d-f) SA; (g-i) HIP treated LPBF samples.

between the different components of the transfer function is shown in Fig. 12.

To reduce the number of fitting parameters, constant values of $\alpha = 0.8$ and $\varepsilon = 12$ were assigned to the part of potential consumed at the F/S interface and the dielectric constant of the barrier layer. For simplicity, the transfer coefficients for each step of the hydrogen reaction, α_i ($i = 1H, -1H, 2H$ and $-2H$) were assumed to be equal to 0.5.

The fitting results are shown in Fig. 4 - Fig. 6 with solid lines and illustrate the good correspondence between experimental data and model predictions. The estimated parameter values are collected in Table 4 as depending on the material and exposure conditions (presence and absence of dissolved hydrogen, as well as after a H₂ - no H₂ - H₂ sequence). It is noteworthy that the parameters estimated in the presence of H₂ are very close to those published in our pre-study [29].

The calculated values of the barrier layer thickness, field strength in the oxide and the metal oxidation rate allow us to estimate the corrosion release rate using the following expression derived within the frames of the MCM [41].

$$\frac{dn_{M^{2+}}(t)}{dt} \approx k_M \exp\left[-\frac{2\alpha_M F \vec{E}}{RT}L\right] \tag{12}$$

Assuming $\alpha_M = 0.1$ as customary for systems involving passive films, the release rate is estimated both in the presence and absence of dissolved hydrogen. The values are collected in Table 5.

The main effect of purging the dissolved hydrogen out of the system is predictably on the kinetic parameters of the hydrogen reaction (the rates of the reduction steps 1H and 2H decrease, whereas those of the oxidation steps −1H and −2H increase). The increase is especially significant for step − 2H (desorption of hydrogen adatoms), i.e. the catalytic effect of the surface towards this reaction becomes important at very low dissolved hydrogen concentrations. There is no discernible effect of the type of material on the rate constants of the hydrogen reaction, thus it can be stated that the kinetics of that interfacial process is not influenced by differences in the oxide structure.

The alloy oxidation parameters (k_M and k_O) at the M/F interface in the presence of dissolved hydrogen are significantly lower for heat-treated LPBF samples when compared to the reference wrought 316 L. This indicates a significantly slower oxidation rate of the LPBF materials. At steady state, the rate of oxide layer dissolution should be equal to that of oxide layer formation. Therefore, the oxide layer dissolution kinetics is considerably faster on wrought material than on heat-treated LPBF materials. Moreover, ejection rate of interstitial cations from the F/S interface and the corrosion release rate from wrought 316 L are significantly higher than from LPBF 316 L.

In the absence of dissolved hydrogen, differences between oxidation and corrosion release rates of the reference material and the LPBF specimens tend to become smaller. An important point is that the oxidation rates are evidently lower in the absence of hydrogen, which can be due to a lower dissolution rate of the barrier oxide at a higher corrosion potential (–0.64 vs. −0.71 V). This can be correlated to the somewhat larger average thickness of the barrier layer in the absence of
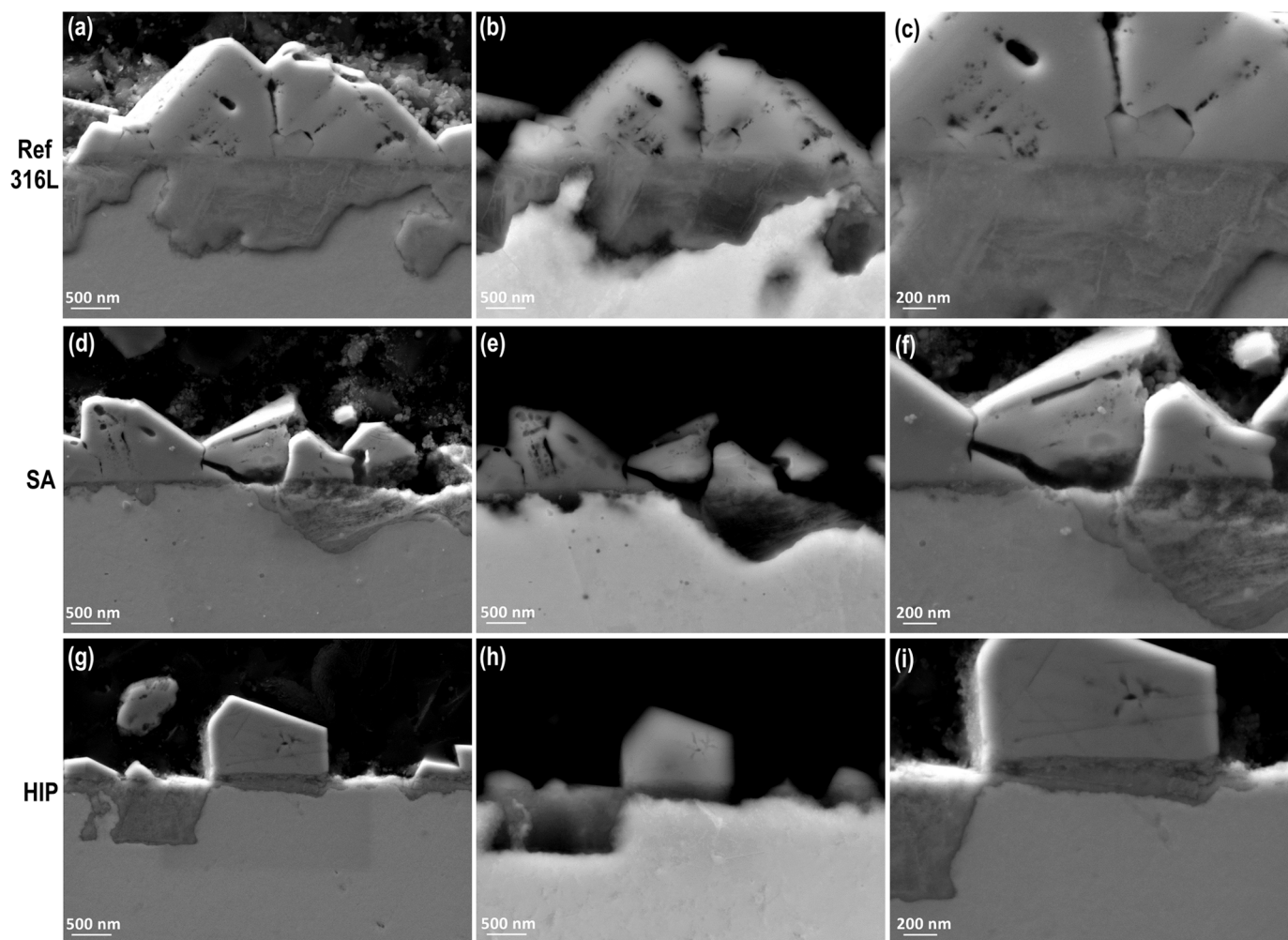
Fig. 8. Cross-sectional SEM-SE and BSE images of the outer and inner oxide layers of LPBF 316 L and wrought 316 L materials after electrochemical measurements in simulated PWR coolant. (a-c) Wrought 316 L; (d-f) SA; (g-i) HIP treated LPBF samples.

hydrogen (i.e. at higher corrosion potential) as estimated from EIS analysis. The increase of barrier layer thickness with potential was observed for wrought nuclear grade 316 L in PWR primary coolant at 280 °C [47].

The magnitudes of the diffusion coefficients of metal cations via interstitial positions and oxygen anions via vacancies in the spinel lattice are comparable for all studied materials. This indicates a similar conduction mechanism in the barrier layer on all of them. The lower field strength in the absence of hydrogen combined with a larger thickness indicates that the potential drop through the barrier layer is not influenced by dissolved hydrogen. Both the capacitance at the oxide/coolant interface ($C_{F/S}$) and the concentration of active sites at the same interface (β) are larger in the absence of hydrogen, indicating higher geometrical and/or energetical roughness of the interface. Summarizing, the differences between the heat-treated LPBF materials and the reference steel are significant in the presence of H$_2$ and tend to be less important in its absence.

Summarizing, high-temperature electrochemical measurements including re-passivation transients, EIS and CV curves at 288 °C revealed differences of electrochemical behavior of the studied materials, particularly between the reference condition and the post heat-treated LPBF samples. Re-passivation rates for the LPBF materials are comparable to those of wrought 316 L, since values of the *cBV* parameter are comparable for all studied steels. Electrochemical impedance data demonstrate that the wrought 316 L exhibits a higher corrosion rate

when dissolved hydrogen is present, as evidenced by a lower impedance magnitude (at the low frequency end) than the LPBF materials. MCM interpretation of EIS data indicates that in the presence of dissolved hydrogen, rate constants of ejection of interstitial cations at the F/S interface and alloy oxidation at the M/F interface exhibit significantly lower values on the LPBF materials than on the reference wrought 316 L, indicating higher oxidation and corrosion release rates, as well as faster oxide dissolution kinetics of the wrought material.

4.2. Correlation to post-exposure characterization

The above quantitative interpretation using the MCM is further confirmed by post-exposure characterization. As revealed in Fig. 7(b-c), partial dissolution was found on the wrought 316 L specimen but not on post heat-treated LPBF 316 L specimens, which indicates a higher stability of the films on the LPBF 316 L materials. The segregation of Cr and Mo to dislocation cell boundaries has been postulated to form micro-galvanic coupling and result in a more stable passive layer [3]. The stability of the passive film formed on stainless steels in PWR high-temperature water environment is a critical factor on the SCC behavior [48].

Cross-sectional microscopy on the post heat-treated LPBF samples reveals an inhomogeneous inner oxide with disperse oxide crystals and large local thickness variations. In contrast, a more uniform inner oxide layer was observed on the nuclear grade wrought 316 L. The thickness of
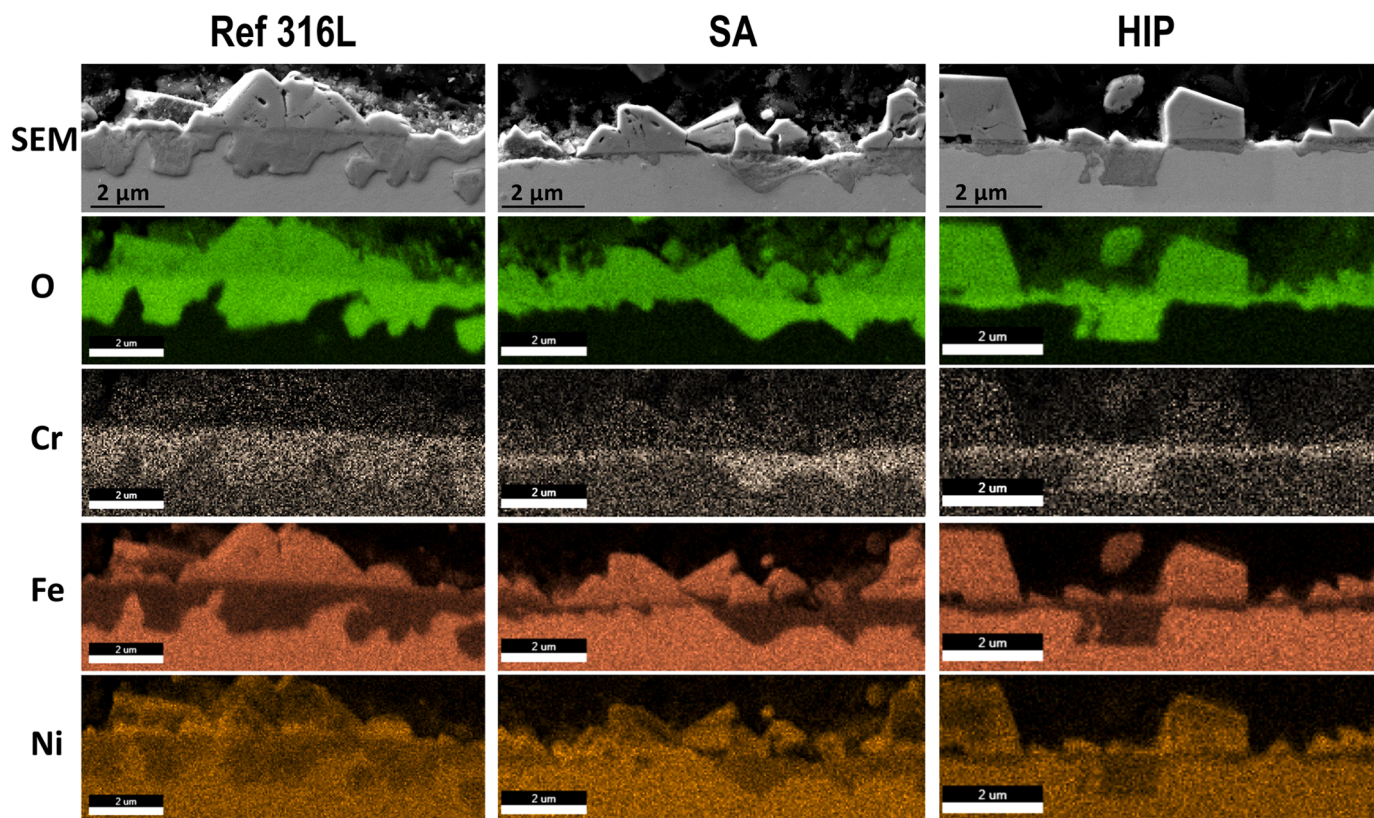
Fig. 9. SEM-EDX mapping of the oxide layer structures on wrought 316 L and LPBF 316 L after the electrochemical measurements in simulated PWR water environment.

the barrier layer on the HIP treated LPBF 316 L corresponds reasonably well to the estimation based on EIS modelling. According to TEM analysis, the inner oxide formation process is directly related to the nano-precipitates in the matrix.

Disperse Cr-enriched inner oxide crystals only nucleate and grow in certain areas in the heat-treated LPBF 316 L materials, indicating a localized oxidation behavior. Nano-precipitates are widely distributed in LPBF 316 L matrix but not in wrought 316 L (see Fig. 13) and contribute to such localized reactions. The works by Chao [49] and Sander [50] revealed a beneficial influence of nanoscale oxide inclusions formed during LPBF progress on the pitting resistance of LPBF 316 over wrought 316 stainless steel. Upon exposure of LPBF materials to high-temperature water, Mn and Cr-rich nano-precipitates near the F/S interface lead to preferential nucleation of Cr-rich inner oxides. Cathodic processes during passivation partially protect the surrounding areas of nucleation points. This is followed by the coarsening of sparsely distributed Cr-rich oxides enclosing the nano-precipitates, leading to the formation of an inhomogeneous inner layer. The smaller area fraction of the inner layer at the M/F interface on LPBF 316 L compared to that on the wrought 316 L indicates slower average layer growth kinetics. Consequently, due to lesser supersaturation and re-precipitation at the F/S interface, less outer oxide particles are formed on LPBF than on wrought 316 L. This hypothesis is in line with a recent study from Tian et al. [51] that highly localized corrosion occurred via dissolution of inclusions along dislocation cell boundaries.

4.3. A hypothesis on the effect of hydrogen

In high-temperature PWR water environment with dissolved hydrogen, Ni remains in the metallic form. TEM results indicate a more pronounced enrichment of Ni at the F/S interfaces on LPBF 316 L materials than on wrought 316 L, thereby limiting Fe dissolution. The

increased Ni concentration in the LPBF materials (as shown in Table 2) catalyzes hydrogen oxidation, resulting in locally faster hydrogen oxidation rate near the anodic sites of Mn- and Cr-rich nano-precipitates. This local activity comes at the expense of other anodic reactions, such as metal dissolution, as the sum of the oxidation currents (Fe dissolution and hydrogen oxidation) should equal the reduction current (the only reduction reaction being that of water). Consequently, the anodic activity of heat-treated LPBF materials is restricted to the nano-precipitates, leading to the formation of an inner oxide with Cr-rich oxide crystals that are sparsely distributed.

In the case of PWR water without hydrogen, Ni is present in oxidized form, and the differences between the electrochemical response of the materials tend to be smaller. Predictably, the importance of hydrogen reactions decreases and the behavior is dominated by the processes of film growth, dissolution and restructuring. The corrosion rates of the investigated materials exhibit a noticeable decrease in the absence of hydrogen. Upon purging hydrogen from the system, the electrochemical properties of the oxide films undergo irreversible changes and do not return to their original state even if initial hydrogen concentration is restored. After hydrogen level restoration, corrosion rates of all studied materials are somewhat lower level than that before hydrogen removal. This result has important consequences for shutdown and startup procedures of PWRs, during which a transition from alkaline / reducing to acid / oxidizing conditions takes place. It also implies that a sudden loss of hydrogen pressure during normal operation would not pose an immediate threat to the construction materials in the primary loop.

5. Conclusions

The electrochemical behavior of two post heat-treated LPBF 316 L materials as compared to a reference nuclear grade wrought 316 L was investigated in a simulated PWR primary coolant with and without
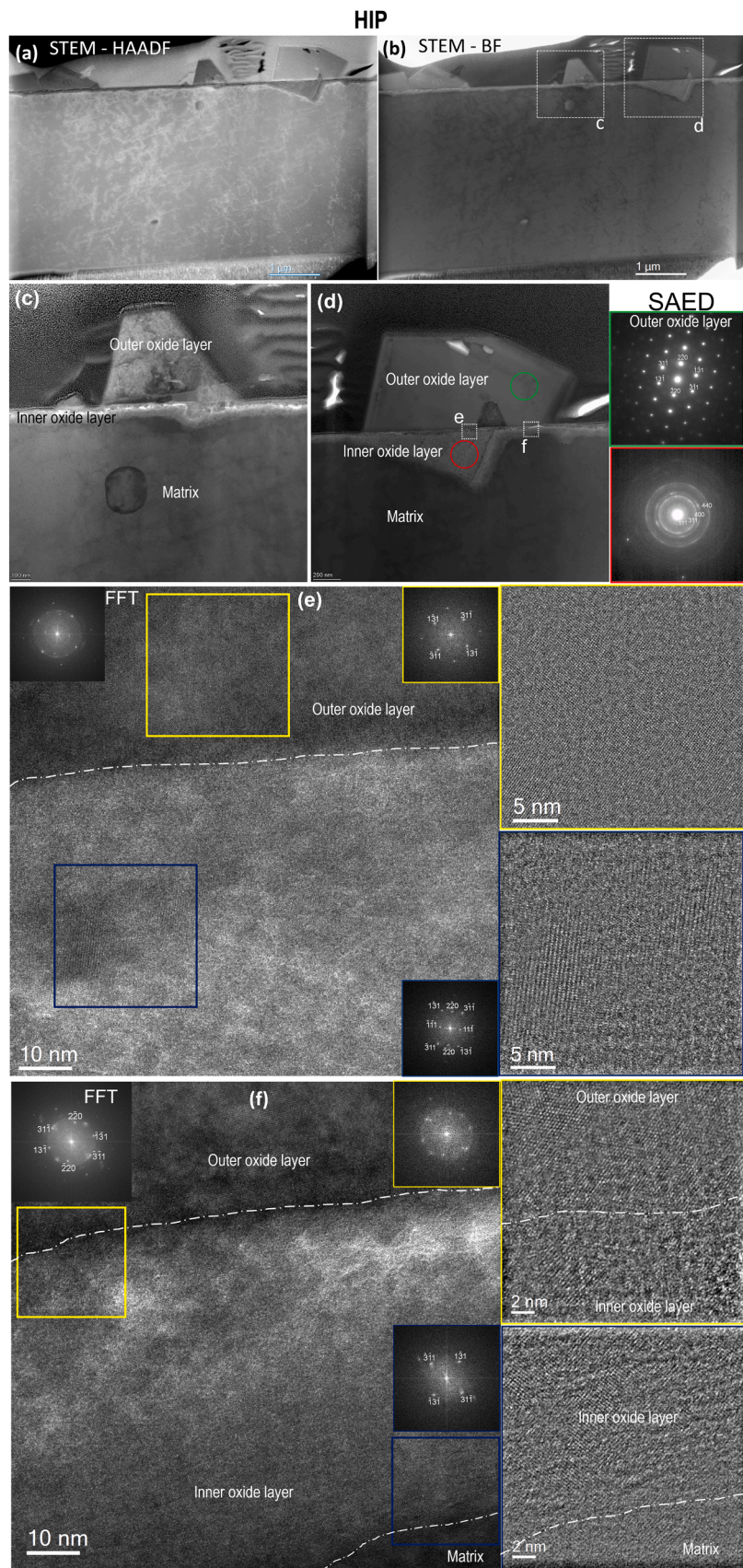
Fig. 10. Overview of HIP sample (a) STEM HAADF image and (b) STEM-BF image. (c) Magnified thin inner oxide layer. (d) Magnified thick inner oxide layer and SAED patterns of outer oxide and inner oxide, respectively. (e) HRTEM image of thick inner oxide area and two insets of magnified HRTEM images and their FFT from outer oxide and inner oxide, respectively. (f) HRTEM image thin inner oxide area and the two insets of magnified HRTEM images and their FFT from the outer oxide/inner oxide interface and M/F interface, respectively.

Fig. 11. (a) STEM-BF and STEM-HAADF images of thick inner oxide area in HIP lamella and EDS line profile (at%) from the marked red arrow in STEM-HAADF image. (b) The elemental map (wt%) of (a). (c) STEM-BF and STEM-HAADF images of thin inner oxide area and EDS line profile (at%) from the marked red arrow in STEM-HAADF image. (d) The elemental map (wt%) of (c).

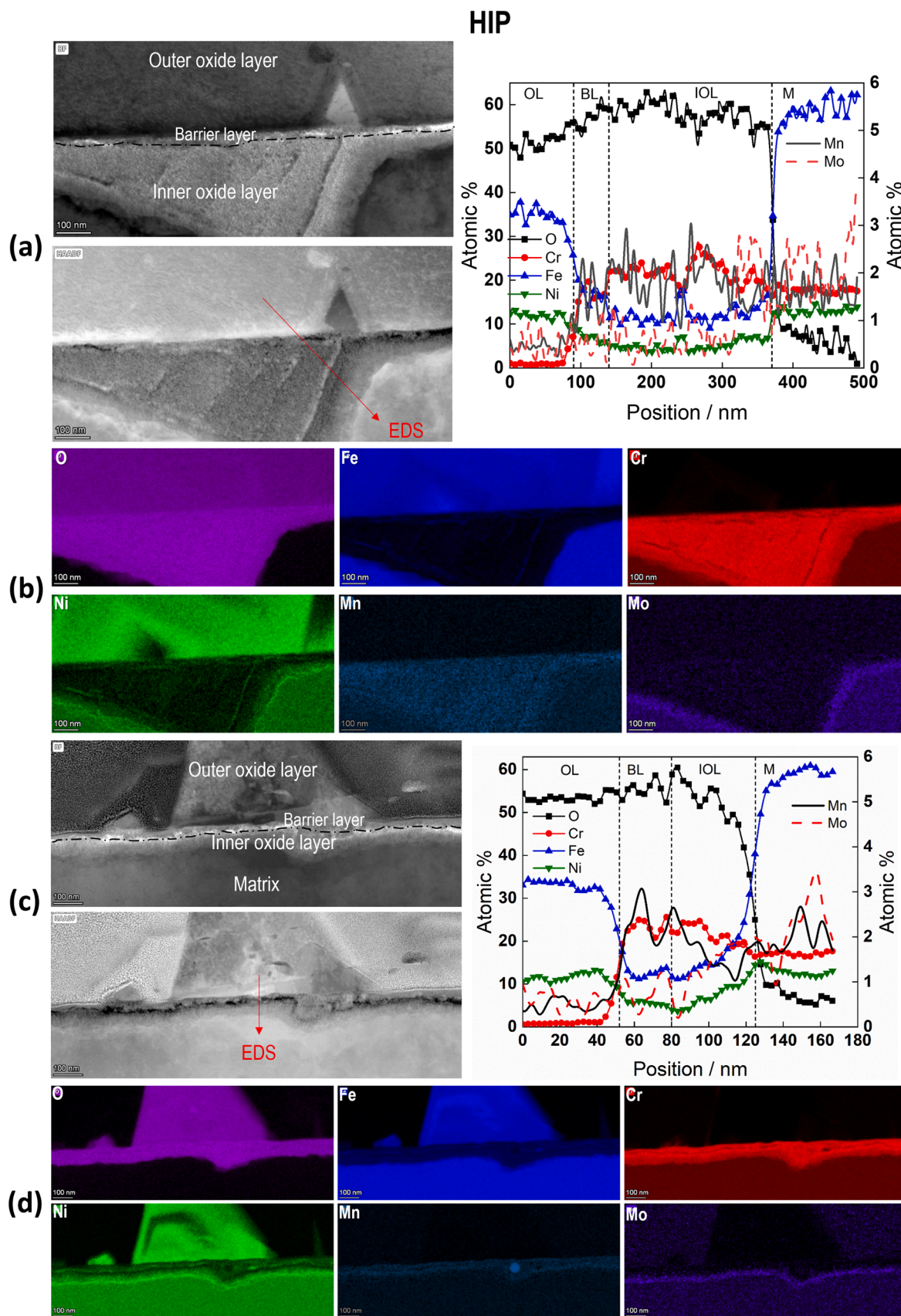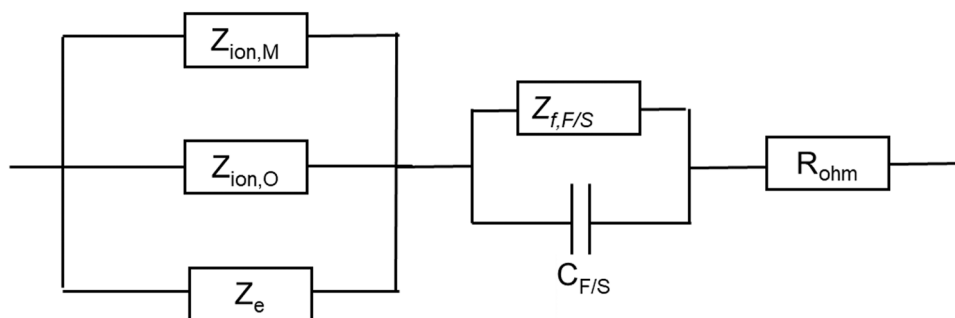**Fig. 12.** Equivalent circuit that illustrates the connection between different components of the transfer function based on the MCM.

Table 4

Summary of the kinetic parameters calculated by fitting the EIS data in the presence and absence of dissolved H2 to the equations of the MCM. Nominal dissolved H2 concentration 1.57 mmol kg-1(H2 stage) and 0.0157 mmol kg-1 (no H2 stage).

Parameter	Wrought 316 L			SA			HIP		
	H_2	no H_2	H_2 after no H_2	H_2	no H_2	H_2 after no H_2	H_2	no H_2	H_2 after no H_2
10^{12} k_M / mol cm^{-2} s^{-1}	10.0 ± 0.8	14.1 ± 0.8	14.1 ± 0.8	$6.0 \pm .0.5$	10 ± 0.8	15 ± 0.9	5.0 ± 0.6	10 ± 0.8	2.0 ± 0.16
10^{12} k_O / mol cm^{-2} s^{-1}	8.0 ± 0.8	7.0 ± 0.6	7.0 ± 0.6	4.5 ± 0.4	4.5 ± 0.4	1.0 ± 0.1	2.4 ± 0.15	4.5 ± 0.4	1.4 ± 0.12
C_{sc} / μF cm^{-2}	12.4 ± 0.8	63.8 ± 5	63.8 ± 5	22.5 ± 2.3	36.4 ± 0.4	30.6 ± 2	23.7 ± 2	18.4 ± 2	39.9 ± 3
L / nm	60.0 ± 4.0	68.2 ± 4.0	68.2 ± 4.0	49 ± 4.0	58.2 ± 4.0	65.0 ± 5.0	46 ± 4.0	59.0 ± 4.0	65.3 ± 4.0
10^8 D_e / cm^2 s^{-1}	3.2 ± 0.3	1.2 ± 0.1	1.2 ± 0.1	5.3 ± 0.3	1.3 ± 0.1	2.0 ± 0.15	5.5 ± 0.3	1.3 ± 0.1	2.1 ± 0.15
R_t / Ω cm^2	9.6 ± 2.3	17.8 ± 3	17.8 ± 3	9.1 ± 2	20.6 ± 3	6.8 ± 1.0	10.7 ± 2	9.5 ± 2	5.6 ± 1.5
$C_{F/S}$ / mF cm^{-2}	4.1 ± 0.3	5.4 ± 0.3	5.4 ± 0.3	4.2 ± 0.3	5.4 ± 0.3	9.7 ± 0.4	2.9 ± 0.2	3.6 ± 0.3	5.3 ± 0.3
10^{10} k_{1H} / mol cm^{-2} s^{-1}	1.1 ± 0.1	0.67 ± 0.07	0.67 ± 0.07	1.0 ± 0.1	0.77 ± 0.07	4.0 ± 0.3	1.1 ± 0.07	1.4 ± 0.08	0.8 ± 0.08
10^{10} k_{2H} / mol cm^{-2} s^{-1}	1.1 ± 0.1	1.2 ± 0.1	1.2 ± 0.1	1.2 ± 0.1	1.2 ± 0.1	0.59 ± 0.05	1.2 ± 0.1	1.2 ± 0.1	0.46 ± 0.05
10^{10} k_{-1H} / mol cm^{-2} s^{-1}	1.3 ± 0.1	0.61 ± 0.05	0.61 ± 0.05	1.3 ± 0.1	0.61 ± 0.05	0.30 ± 0.04	1.2 ± 0.1	0.61	0.90 ± 0.1
10^4 k_{-2H} / cm s^{-1}	1.3 ± 0.1	250 ± 20	250 ± 20	1.3 ± 0.1	250 ± 20	90 ± 6	1.3 ± 0.12	250 ± 20	110 ± 10
10^9 k_{2M} / cm s^{-1}	3.1 ± 0.3	3.4 ± 0.3	3.4 ± 0.3	3.7 ± 0.3	3.4 ± 0.3	1.4 ± 0.13	1.8 ± 0.16	3.5 ± 0.3	4.1 ± 0.4
10^9 k_{2O} / cm s^{-1}	2.1 ± 0.2	1.3 ± 0.15	1.3 ± 0.15	2.1 ± 0.2	1.3 ± 0.12	1.2 ± 0.11	2.1 ± 0.2	1.3 ± 0.12	3.0 ± 0.2
β / nmol cm^{-2}	5.2 ± 0.3	50 ± 5	50 ± 5	6.4 ± 0.5	30 ± 2.5	10 ± 1	6.5 ± 0.5	44 ± 3	10 ± 1
10^{17} D_M / cm^2 s^{-1}	3.0 ± 0.2	2.4 ± 0.2	2.4 ± 0.2	2.4 ± 0.2	2.4 ± 0.2	3.0 ± 0.2	2.4 ± 0.2	2.5 ± 0.2	3.7 ± 0.3
10^{17} D_O / cm^2 s^{-1}	2.0 ± 0.2	2.0 ± 0.2	2.0 ± 0.2	2.0 ± 0.2	2.0 ± 0.2	4.1 ± 0.3	2.0 ± 0.2	2.0 ± 0.2	3.1 ± 0.25
$\vec{E}$ / kV cm^{-1}	95 ± 7	64 ± 7	64 ± 7	103 ± 8	66 ± 6	67.8 ± 6	120 ± 9	68 ± 6	65.7 ± 5.5

Table 5

Corrosion release rates of the studied materials (mol cm-2 s-1) in the presence and absence of dissolved hydrogen.

Material / Condition	H_2	no H_2	H_2 after no H_2
Wrought 316L	6.1×10^{-12}	1.3×10^{-12}	1.6×10^{-12}
SA	3.1×10^{-12}	9.8×10^{-13}	1.2×10^{-12}
HIP	2.4×10^{-12}	9.2×10^{-13}	1.6×10^{-12}

dissolved hydrogen. The following conclusions can be drawn from this work:

- Re-passivation rates of the steels are roughly similar, whereas EIS measurements conducted at 288 °C reveal that wrought 316 L material exhibits a higher corrosion rate than LPBF 316 L materials in the presence of dissolved hydrogen.
- Unlike the uniform inner oxide layer formed on wrought 316 L, an inner oxide layer with Cr-rich inner oxide crystals that are sparsely distributed and a large variation in thickness is observed on LPBF 316 L materials. In spite of a considerable evolution in the microstructure with heat treatments, there is no significant difference in corrosion rate in the HIP and SA treated LPBF 316 L materials.
- The removal of hydrogen from the system leads to a reduction in the corrosion rate of the studied materials. This indicates the importance of hydrogen evolution/oxidation reactions in the corrosion process. However, the presence/absence of hydrogen does not interfere with the estimation of kinetic and transport parameters related to film growth and corrosion release.
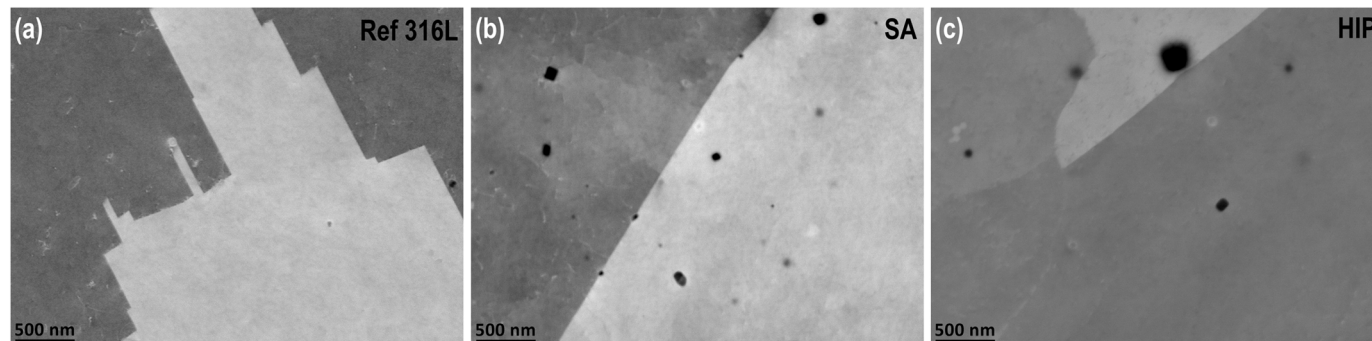

Fig. 13. SEM backscattered electron images for (a) wrought 316 L, (b) SA and (c) HIP materials.

- Irreversible changes occur once hydrogen is purged from the system, and the electrochemical properties of the oxide films do not revert to their initial state, even when the hydrogen concentration is restored. After increasing the hydrogen level to the starting one, the corrosion rates of all the studied materials stay at a somewhat lower level than before hydrogen removal. Based on the experimental and calculation results, a hypothesis that correlates the effect of hydrogen with the oxidation state of Ni in the barrier layer and at the oxide/solution interface is proposed.

- As revealed by the TEM on the HIP treated LPBF 316 L material, nano-precipitates formed during LPBF process significantly affect the oxide formation and elemental segregation in the inner oxide layer.

CRediT authorship contribution statement

M. Bojinov: Conceptualization, Data curation, Formal analysis, Investigation, Methodology, Writing – original draft, Writing – review & editing. **T. Saario:** Data curation, Formal analysis, Investigation, Methodology, Writing – review & editing. **Y. Ge:** Data curation, Formal analysis, Investigation, Methodology, Writing – original draft, Writing – review & editing. **L. Chang:** Conceptualization, Methodology, Writing – review & editing. **Z. Que:** Conceptualization, Data curation, Formal analysis, Investigation, Methodology, Project administration, Resources, Writing – original draft, Writing – review & editing.

Declaration of Competing Interest

The authors declare that they have no known competing financial interests or personal relationships that could have appeared to influence the work reported in this paper.

Data availability

The data that support the findings of this study are available from the corresponding author upon reasonable request.

Acknowledgements

References

[1] H. Springer, C. Baron, A. Szczepaniak, E. Jägle, M. Wilms, A. Weisheit, D. Raabe, Efficient additive manufacturing production of oxide- and nitride-dispersion-strengthened materials through atmospheric reactions in liquid metal deposition, Mater. Des. 111 (2016) 60–69.

[2] G. Wang, H. Ouyang, C. Fan, Q. Guo, Z. Li, W. Yan, Z. Li, The origin of high-density dislocations in additively manufactured metals, Mater. Res. Lett. 8 (8) (2020) 283–290.

[3] D. Kong, C. Dong, S. Wei, X. Ni, L. Zhang, R. Li, L. Wang, C. Man, X. Li, About metastable cellular structure in additively manufactured austenitic stainless steels, Addit. Manuf. 38 (101804) (2021).

[4] T. Ngo, A. Kashani, G. Imbalzano, K. Nguyen, D. Hui, Additive manufacturing (3D printing): a review of materials, methods, applications and challenges, Compos. Part B 143 (2018) 172–196.

[5] Y. Sun, A. Moroz, K. Alrbaey, Sliding wear characteristics and corrosion behaviour of selective laser melted 316L stainless steel, J. Mater. Eng. Perform. 23 (2014) 518–526.

[6] Z. Sun, X. Tan, S. Tor, Selective laser melting of stainless steel 316L with low porosity and high build rates, Mater. Des. 104 (2016) 197–204.

[7] X. Lou, M. Song, P. Emigh, M. Othon, P. Andresen, On the stress corrosion crack growth behaviour in high temperature water of 316L stainless steel made by laser powder bed fusion additive manufacturing, Corros. Sci. 128 (2017) 140–153.

[8] Z. Que, T. Riipinen, S. Goel, A. Revuelta, T. Saario, K. Sipilä, A. Toivonen, SCC behaviour of laser powder bed fused 316L stainless steel in high-temperature water at 288 °C, Corros. Sci. 214 (111022) (2023).

[9] Westinghouse Creates and Installs Industry's First 3D-Printed Fuel Debris Filter for Nuclear Power Plants, Westinghouse Electric Company, July 2022. ([Online]. 〈https://info.westinghousenuclear.com/news/westinghouse-creates-and-installs-industrys-first-3d-printed-fuel-debris-filter-for-nuclear-power-plants?utm_campaign=ogsocial&utm_content=1655125790&utm_medium=social&utm_source=linkedin〉). (Accessed July 2022).

[10] M. Yeganeh, M. Rezvani, S. Laribaghal, Electrochemical behavior of additively manufactured 316L stainless steel in H2SO4 solution containing methionine as an amino acid, Colloids Surf. A Physicochem. Eng. Asp. 627 (127120) (2021).

[11] M. Karimi, M. Yeganeh, S. Zaree, M. Eskandari, Corrosion behavior of 316L stainless steel manufactured by laser powder bed fusion (L-PBF) in an alkaline solution, Opt. Laser Technol. 138 (106918) (2021).

[12] G. Sander, J. Tan, P. Balan, O. Gharbi, D. Feenstra, L. Singer, S. Thomas, R. Kelly, J. Scully, N. Birbilis, Corrosion of additively manufactured alloys: a review, Corrosion 74 (18) (2018).

[13] R. Revilla, M. Calster, M. Raes, G. Arroud, F. Andreatta, L. Pyl, P. Guillaume, I. Graeve, Microstructure and corrosion behavior of 316L stainless steel prepared using different additive manufacturing methods: a comparative study bringing insights into the impact of microstructure on their passivity, Corros. Sci. 176 (108914) (2020).

[14] R. Revilla, B. Wouters, F. Andreatta, A. Lanzutti, L. Fedrizzi, I. De Graeve, EIS comparative study and critical Equivalent Electrical Circuit (EEC) analysis of the native oxide layer of additive manufactured and wrought 316L stainless steel, Corros. Sci. 167 (108480) (2020).

[15] M. Lodhi, K. Deen, M. Greenlee-Wacker, W. Haider, Additively manufactured 316L stainless steel with improved corrosion resistance and biological response for biomedical applications, Addit. Manuf. 27 (2019) 8–19.

[16] C. Man, C. Dong, T. Liu, D. Kong, D. Wang, X. Li, The enhancement of microstructure on the passive and pitting behaviors of selective laser melting 316L SS in simulated body fluid, Appl. Surf. Sci. 467–468 (2019) 193–205.

[17] J. Nie, L. Wei, Y. Jiang, Q. Li, H. Luo, Corrosion mechanism of additively manufactured 316 L stainless steel in 3.5 wt% NaCl solution, Mater. Today Commun. 26 (101648) (2021).

[18] J. Trelewicz, G. Halada, O. Donaldson, G. Manogharan, Microstructure and corrosion resistance of laser additively manufactured 316L stainless steel, JOM 68 (2016) 850–859.

[19] Y. Kok, X. Tan, P. Wang, M. Nai, N. Loh, E. Liu, S. Tor, Anisotropy and heterogeneity of microstructure and mechanical properties in metal additive manufacturing: a critical review, Mater. Des. 139 (2018) 565–586.

[20] M. Song, M. Wang, X. Lou, R. Rebak, G. Was, Radiation damage and irradiation-assisted stress corrosion cracking of additively manufactured 316L stainless steels, J. Nucl. Mater. 513 (2019) 33–44.

[21] X. Lou, M. Othon, R. Rebak, Corrosion fatigue crack growth of laser additively-manufactured 316L stainless steel in high temperature water, Corros. Sci. 127 (2017) 120–130.

[22] C. Zhou, S. Hu, Q. Shi, H. Tao, Y. Song, J. Zheng, P. Xu, L. Zhang, Improvement of corrosion resistance of SS316L manufactured by selective laser melting through subcritical annealing, Corros. Sci. 164 (108353) (2020).

[23] M. Shimada, H. Kokawa, Z. Wang, Optimization of grain boundary character distribution for intergranular corrosion resistant 304 stainless steel by twin-induced grain boundary engineering, J. Acta Mater. 50 (2002) 2331–2341.

[24] M. Laleh, A. Hughes, W. Xu, P. Cizek, M. Tan, Unanticipated drastic decline in pitting corrosion resistance of additively manufactured 316L stainless steel after high-temperature post-processing, Corros. Sci. 165 (108412) (2020).

[25] A. Ettefagh, S. Guo, Electrochemical behavior of AISI316L stainless steel parts produced by laser-based powder bed fusion process and the effect of post annealing process, Addit. Manuf. 22 (2018) 153–156.

[26] D. Kong, C. Dong, X. Ni, L. Zhang, J. Yao, C. Man, X. Cheng, K. Xiao, X. Li, Mechanical properties and corrosion behavior of selective lasermelted 316L stainless steel after different heat treatment processes, J. Mater. Sci. Technol. 35 (2019) 1499–1507.

[27] Q. Xiao, J. Chen, H. Lee, C. Jang, K. Jang, Effect of heat treatment on corrosion behaviour of additively manufactured 316L stainless steel in high-temperature water, Corros. Sci. 210 (110830) (2023).

[28] S. Zhang, S. Wang, X. Feng, Z. Ning, J. Hou, W. Kuang, Insights into the stress corrosion cracking resistance of a selective laser melted 304L stainless steel in high-temperature hydrogenated water, Acta Mater. 244 (118561) (2023).

[29] Z. Que, L. Chang, T. Saario, M. Bojinov, Localised electrochemical processes on laser powder bed fused 316L with various heat treatments in high-temperature water, Addit. Manuf. 60 (103205) (2022).

[30] T. Terachi, T.K. Yamada, K. Fukuya, Corrosion behavior of stainless steels in simulated PWR primary water—effect of chromium content in alloys and dissolved hydrogen, J. Nucl. Sci. Technol. 45 (4) (2008) 975–984.

[31] M. Dumerval, S. Perrin, L. Marchetti, M. Tabarant, F. Jomard, Y. Wouters, Hydrogen absorption associated with the corrosion mechanism of 316L stainless steels in primary medium of Pressurized Water Reactor (PWR), Corros. Sci. 85 (2014) 251–257.

[32] L.-F. Zhang, J.-M. Wang, High-temperature electrochemical corrosion behavior of Fe-Cr-Ni Alloys in simulated pressurized water reactor water, Corrosion 74 (4) (2017) 415–423.

[33] J. Chen, Q. Xiao, Z. Lu, X. Ru, H. Peng, Q. Xiong, Characterization of interfacial reactions and oxide films on 316L stainless steel in various simulated PWR primary water environments, J. Nucl. Mater. 489 (2017) 137–149.

[34] X. Zhong, S. Xia, J. Xu, T. Shoji, The oxidation behavior of 316L in simulated pressurized water reactor environments with cyclically changing concentrations of dissolved oxygen and hydrogen, J. Nucl. Mater. 511 (2018) 417–427.

[35] L. Dong, Q. Peng, Z. Zhang, T. Shoji, E.-H. Han, W. Ke, Effect of dissolved hydrogen on corrosion of 316NG stainless steel in high temperature water, Nucl. Eng. Des. 295 (2015) 403–414.

[36] J. Reijonen, R. Björkstrand, T. Riipinen, Z. Que, S. Metsä-Kortelainen, M. Salmi, Cross-testing laser powder bed fusion production machines and powders: variability in mechanical properties of heat-treated 316L stainless steel, Mater. Des. 204 (109684) (2021).

[37] Nuclear Grade Stainless Steel Procurement, Manufacturing, and Fabrication Guidelines, Electric Power Research Institute, Document #84-MG-18, Palo Alto, California, 1985.

[38] C. You, M.A. Zabara, M.E. Orazem, 和 B. Ulgut, Application of the Kramers–Kronig relations to multi-sine electrochemical impedance measurements, J. Electrochem. Soc., 卷 167 (2020), 020515.

[39] Roine, A.; Anttila, K., HSC 6.0 - Chemical Reaction and Equilibrium Software with Extensive Thermochemical Database and Flowsheet Simulation, Outokumpu Research Ltd, 2006.

[40] I. Betova, M. Bojinov, T. Ikäläinen, T. Saario, K. Sipilä, Corrosion of alloy 690 in simulated steam generator crevices – effect of applied potential, pH and Pb addition, J. Electrochem. Soc. 169 (021502) (2022).

[41] M. Bojinov, E. Jäppinen, T. Saario, K. Sipilä, A. Toivonen, Effect of lead and applied potential on corrosion of carbon steel in steam generator crevice solutions, Corros. Sci. 159 (2019) 108–117.

[42] Z. Que, M. Heczko, I. Kuběna, H. Seifert, P. Spätig, Microstructural characterization of the synergic effects of dynamic strain ageing and hydrogen on fracture behaviour of low-alloy RPV steels in high-temperature water environments, Mater. Charact. 165 (110405) (2020).

[43] S. Zhang, F. Bi, T. Wu, Y. Wang, Z. Que, L. Chang, Microstructural investigation of the effect of hot-isostatic-pressing treatment on a laser powder bed fused type 316L stainless steel, Mater. Charact. 197 (112716) (2023).

[44] E.-A. Cho, C.-K. Kim, J.-S. Kim, H.-S. Kwon, Quantitative analysis of re-passivation kinetics of ferritic stainless steels based on the high field ion conduction model, Electrochim. Acta 45 (2000) 1933–1942.

[45] J. Liu, J. Wang, Z. Zhang, H. Zheng, Repassivation behavior of alloy 690TT in simulated primary water at different temperatures, J. Mater. Sci. Technol. 68 (3) (2021) 227–235.

[46] J. Wang, E.-H. Han, J. Wang, The repassivation kinetics study of Alloy 800 in high-temperature pressurized water, Electrochem. Commun. 60 (11) (2015) 100–103.

[47] I. Betova, M. Bojinov, P. Kinnunen, K. Lundgren, T. Saario, Influence of Zn on the oxide layer on AISI 316L(NG) stainless steel in simulated pressurised water reactor coolant, Electrochim. Acta 54 (3) (2009) 1056–1069.

[48] R. Soulas, M. Cheynet, E. Rauch, T. Neisius, L. Legras, C. Domain, Y. Brechet, TEM investigations of the oxide layers formed on a 316L alloy in simulated PWR environment, J. Mater. Sci. 48 (2013) 2861–2871.

[49] Q. Chao, V. Cruz, S. Thomas, On the enhanced corrosion resistance of a selective laser melted austenitic stainless steel, J. Scr. Mater. 141 (2017) 94–98.

[50] G. Sander, S. Thomas, V. Cruz, M. Jurg, N. Birbilis, X. Gao, M. Brameld, C. Hutchinson, On the corrosion and metastable pitting characteristics of 316L stainless steel produced by selective laser melting, Electrochem. Soc. Interface 164 (2017) C250–C257.

[51] M. Tian, J. Choundraj, T. Voisin, Y. Wang, J. Kacher, Discovering the nanoscale origins of localized corrosion in additive manufactured stainless steel 316L by liquid cell transmission electron microscopy, Corros. Sci. 208 (110659) (2022).